Effect of an input beam's shape and curvature on the nonlinear effects in graded-index fibers

AMIRA S. AHSAN* ID **AND GOVIND P. AGRAWAL** ID

The Institute of Optics, University of Rochester, Rochester, New York 14627, USA
*Corresponding author: aahsan@ur.rochester.edu

We present a general framework capable of describing the nonlinear propagation of pulsed optical beams of arbitrary shapes and phase fronts inside a graded-index (GRIN) fiber. The main assumption made is that the spatial self-imaging features of the beam are not affected by the temporal evolution of optical pulses. A propagation kernel known from the work done in the 1970s is used to obtain a distance-dependent nonlinear coefficient that captures all spatial effects within an effective nonlinear Schrödinger equation. We consider three specific beam shapes (Gaussian, circular, and square) to study the impact of the shape, position, and curvature of optical beams on the complex spatiotemporal dynamics specific to GRIN fibers. In particular, we focus on the impact of an input beam's shape on the modulation-instability sidebands and the generation of multiple dispersive waves when higher-order solitons form inside a GRIN fiber. The results of our numerical analysis indicate that for beam widths chosen to yield the same value of the effective mode area at the input end of the fiber, the nonlinear effects are pronounced considerably when a Gaussian beam is launched into the fiber. We also found that even though the self-imaging period is doubled when an off-centered Gaussian beam is launched into a GRIN fiber, it does not affect the nonlinear evolution because the effective beam area still maintains the same periodicity, as long as the shift in the beam's center is not so large that it does not remain confined to the fiber's core.   © 2020 Optical Society of America

https://doi.org/10.1364/JOSAB.379253

1. INTRODUCTION

Study of the nonlinear optical phenomena inside graded-index (GRIN) multimode fibers has attracted considerable attention in recent years [1–3]. Geometric parametric instability (GPI), a kind of spatiotemporal instability occurring in GRIN fibers, was studied first in 2003 [4] and observed in a 2016 experiment [5]. Multimode solitons, whose formation attracted attention during the 1990s [6–8], have also been observed and studied in recent years [9–11]. Considerable effort has been dedicated to examine the spatial-beam cleanup induced by the Kerr effect [12–15]. Supercontinuum generation inside GRIN fibers is also being studied [16–19]. In most of these studies, the shape of the input beam is taken to be Gaussian, perhaps because most lasers emit Gaussian-like beams. Moreover, it is assumed that the beam is launched into a GRIN fiber such that its phase front is planar (no curvature) at the input end of the fiber. So far, almost nothing is known about how the nonlinear effects inside a GRIN fiber are affected when the shape and curvature of the input beam differ from that of a Gaussian beam. The reason appears to be that the propagation problem is perceived to be difficult for non-Gaussian input beams. Indeed, the variational method used in 1992 assumed a Gaussian beam to study the

propagation of a continuous-wave (CW) beam inside GRIN fibers [20].

The phenomenon of self-imaging, leading to periodic restoration of the input shape of a Gaussian beam has been found to play a crucial role in governing the nonlinear evolution of short optical pulses inside GRIN fibers [2]. However, it is well known that self-imaging is a linear property of any GRIN medium for an input beam of arbitrary shape [21–23]. A modal-expansion approach used in 1974 shows that the output field at any point inside the GRIN fiber can be obtained, without any reference to the fiber modes, using a propagation kernel that is similar in nature to the one occurring in diffraction theory [21]. This kernel can be used to describe evolution of optical beams of arbitrary shapes inside a GRIN fiber and shows that all beam shapes undergo self-imaging in a periodic fashion, and this period does not depend on the beam shape or the phase-front curvature. In this paper, we use this kernel to study the impact of an input beam's shape and curvature on the nonlinear effects in GRIN fibers.

The paper is organized as follows. In Section 2, we review the self-imaging theory and use it to show that the effective nonlinear Schrödinger (NLS) equation, derived in the past for input Gaussian beams and containing the nonlinear parameter

$\gamma(z)$ that oscillates periodically along the fiber's length [24], can be extended to pulsed beams of arbitrary spatial shapes. The effects of beam shape appear in this equation through the form of spatial oscillations of $\gamma(z)$. In Section 3, we compare the $\gamma(z)$ oscillations for a Gaussian beam to the beams whose intensity is uniform over a circular or square region. We also consider the effects of a beam whose center is shifted from the center of the fiber core. This case is interesting because a much larger number of modes of the GRIN fiber are excited in view of the absence of radial symmetry. In Section 4, we focus on the effects of input beam shape on two major nonlinear phenomena: creation of multiple sidebands through GPI or modulation instability and evolution of higher-order solitons leading to the formation of multiple dispersive waves. The effects of a curved phase front are studied in Section 5, where we show that any curvature affects the $\gamma(z)$ oscillations significantly and breaks the axial symmetry such that the minimum beam compression does not occur in the middle of the self-imaging period. We also discuss how the phase-front curvature affects the evolution of higher-order solitons inside GRIN fibers. The main results are summarized in the final section of this paper.

2. SELF-IMAGING OF PULSED OPTICAL BEAMS

We first consider the linear propagation of a weak CW beam of frequency ω inside a GRIN fiber and neglect the nonlinear effects. The refractive index of the GRIN fiber is assumed to decrease radially inside the core of radius a from its value n_1 at the center to the cladding index n_c as [25]

$$n^2(x, y) = n_1^2[1 - 2\Delta(\rho/a)^2], \quad \rho = \sqrt{x^2 + y^2}, \quad \textbf{(1)}$$

where $\Delta = (n_1 - n_c)/n_1$ plays an important role and is defined in the same way as for step-index fibers [26]. The modes of GRIN fibers are obtained by solving the Helmholtz equation for the electric field $\tilde{E}$ in the frequency domain:

$$\nabla^2 \tilde{\mathbf{E}} + n^2(x, y)k_0^2 \tilde{\mathbf{E}} = 0, \quad \textbf{(2)}$$

where $k_0 = \omega/c$. This equation can be solved analytically to find the optical modes of a GRIN fiber in the form of Hermite–Gauss functions [25], if we assume that the index profile in Eq. (1) applies for all values of ρ.

Any optical beam with the input field $\tilde{E}(x, y, 0)$, in general, excites multiple fiber modes that propagate with different propagation constants β_{mn}, where m and n are two integers. If we denote the corresponding fiber modes by $F_{mn}(x, y)$, the optical field $E(x, y, z)$ at any point inside the GRIN fiber can be written as

$$\tilde{E}(x, y, z) = \sum_m \sum_n c_{mn} F_{mn}(x, y) \exp(i\beta_{mn}z), \quad \textbf{(3)}$$

where the sum extends over the whole range of the two integers ($m, n = 0$ to ∞). We can find the expansion coefficients c_{mn} in terms of $E(x, y, 0)$:

$$c_{mn} = \iint_{-\infty}^{\infty} F_{mn}^*(x, y)\tilde{E}(x, y, 0)\mathrm{d}x\mathrm{d}y. \quad \textbf{(4)}$$

Substituting c_{mn} into Eq. (3), we can sum the double series following Ref. [21] to find $\tilde{E}(x, y, z)$ in terms of a propagation kernel:

$$\tilde{E}(x, y, z) = \iint_{-\infty}^{\infty} K(x, x'; y, y')\tilde{E}(x', y', 0)\mathrm{d}x'\mathrm{d}y', \quad \textbf{(5)}$$

where the propagation kernel $K(x, x'; y, y')$ is given by

$$K(x, x'; y, y') = \frac{\beta}{2\pi i}\left(\frac{b}{\sin(bz)}\right)e^{i\psi}$$

$$\times \exp\left[\frac{i}{2}\beta b \cot(bz)(x'^2 + y'^2)\right.$$

$$\left. - \frac{i\beta b}{\sin(bz)}(xx' + yy')\right]. \quad \textbf{(6)}$$

Here, $\beta = n_1 k_0$, $b = \sqrt{2\Delta}/a$, and the phase ψ is given by

$$\psi(x, y, z) = \beta z + \frac{1}{2}\beta b \cot(bz)(x^2 + y^2). \quad \textbf{(7)}$$

The self-imaging property of the GRIN fiber arises from the kernel in Eq. (6). It can be shown [3] that the kernel reduces to the product of two delta functions at integer multiples of the period $2\pi/b$:

$$K(x, x'; y, y') = \delta(x - x')\delta(y - y')e^{i\beta z}. \quad \textbf{(8)}$$

Hence, at distances $z = 2m\pi/b$, where m is an integer, the output field $\tilde{E}(x, y, z)$ is identical to the input field $\tilde{E}(x, y, 0)$. Moreover, a mirrored image of the input field is formed at shorter distances $z = n\pi/b$, where n can be any odd integer. Thus, for radially symmetric input fields such as a Gaussian beam, the self-imaging period is given by

$$z_p = \pi/b = \pi a/\sqrt{2\Delta}. \quad \textbf{(9)}$$

For GRIN fibers, typically $a = 25$ μm and $\Delta = 0.01$, resulting in a self-imaging period of <1 mm.

The important question is how the self-imaging behavior changes when the nonlinear contribution $n_2|E|^2$ to the refractive index is not negligible, where n_2 is the Kerr coefficient and $|E|^2$ is the local intensity. It was shown in 1992 using a variational technique that the self-imaging of a Gaussian beam is not affected much by the self-focusing induced by the Kerr nonlinearity [20], as long as the input power remains well below the critical power required for beam collapse. This conclusion holds for optical beams of all shapes. As the value P_{cr} exceeds 2 MW for silica glass at wavelengths near 1 μm, self-imaging should not be affected much by the self-focusing effects for peak-power levels ∼100 kW [24]. However, for pulsed optical beams, the temporal and spectral evolutions of pulses are affected considerably by the spatial self-imaging of the beam. This is what we focus on in this paper.

The temporal evolution of pulsed optical beams is governed by a multi-dimensional nonlinear equation taking the form [24]

$$i\frac{\partial E}{\partial z} + \frac{1}{2\beta_0}\nabla_T^2 E - \frac{\beta_2}{2}\frac{\partial^2 E}{\partial t^2} - \beta_0\Delta\frac{\rho^2}{a^2}E + \frac{n_2\omega_0}{c}|E|^2 E = 0, \quad \textbf{(10)}$$

where $\beta_0 = \beta(\omega_0)$, ∇_T^2 is the transverse Laplacian operator, and β_2 takes into account the group-velocity dispersion (GVD).

Although this equation can be solved numerically, such an approach requires considerable computational resources. It was found in 2017 that it can be reduced to a much simpler equation [24], similar to that used for single-mode fibers, in the regime in which temporal dynamics of the pulse does not significantly affect spatial evolution of the pulsed beam. Using $E(\mathbf{r}, t) = F(x, y, z)A(z, t)$, where $F(x, y, z)$ governs the spatial shape of the beam and $A(z, t)$ represents its temporal evolution along the fiber, the effective NLS equation has the form

$$\frac{\partial A}{\partial z} + i\frac{\beta_2}{2}\frac{\partial^2 A}{\partial t^2} = i\bar{\gamma}(z)|A|^2 A. \quad \textbf{(11)}$$

Its sole new feature compared to the standard NLS equation is that the nonlinear parameter $\bar{\gamma}(z)$ changes along the GRIN fiber's length in response to the spatial beam-width oscillations induced by spatial self-imaging. We write this z dependence in the form

$$\bar{\gamma}(z) = \frac{\omega_0 n_2}{c\, A_{\text{eff}}(z)} = \frac{\gamma}{f(z)}, \quad f(z) = \frac{A_{\text{eff}}(z)}{A_{\text{eff}}(0)}, \quad \textbf{(12)}$$

where the effective beam area $A_{\text{eff}}(z)$ is defined as

$$A_{\text{eff}}(z) = \frac{\left(\iint |F(x, y, z)|^2 \mathrm{d}x\mathrm{d}y\right)^2}{\iint |F(x, y, z)|^4 \mathrm{d}x\mathrm{d}y} = A_{\text{eff}}(0) f(z), \quad \textbf{(13)}$$

and $\gamma = \omega_0 n_2/c\, A_{\text{eff}}(0)$ is defined using the input value of A_{eff}. In essence, $f(z)$ governs the self-imaging induced changes in the effective beam area.

3. SHAPE-DEPENDENT NONLINEAR ENHANCEMENT

The shape and size of an optical beam change along a GRIN fiber because of the graded nature of the refractive index inside such a fiber. In particular, the beam undergoes a compression phase before it recovers its original shape. Since the effective beam area is reduced during the compression phase, the nonlinear effects are enhanced in a periodic fashion. Equation (13) shows how the enhancement factor $f^{-1}(z)$ depends on the beam shape governed by the function $F(x, y, z)$. This function can be calculated for any input beam using the propagation kernel given in Eq. (6). In this section, we calculate $f(z)$ for three specific beam shapes and compare the extent of nonlinearity enhancement for them.

A. Gaussian Beam

Consider first a Gaussian beam centered on the input facet of a GRIN fiber. The input field $E(x', y', 0)$ of such a beam has the form

$$E(x', y', 0) = A_0 \exp\left(-\frac{x'^2 + y'^2}{2w_0^2}\right), \quad \textbf{(14)}$$

where A_0 is the peak amplitude and w_0 is the 1/e width of the Gaussian beam (full width at half maximum about $1.665w_0$). The output field at a distance z is obtained by inserting this input field into Eq. (5) and evaluating the two integrals using the known result
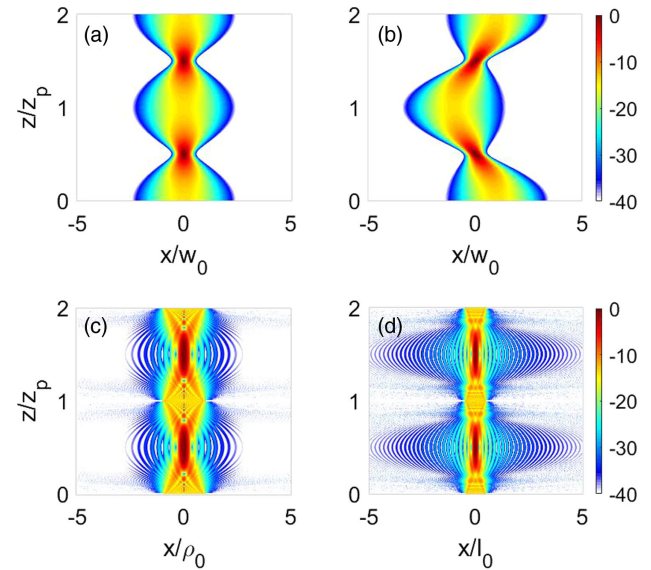
Fig. 1. Evolution over two self-imaging periods of four specific input beams: (a) Gaussian; (b) off-centered Gaussian; (c) constant intensity over a circular region; (d) constant intensity over a square region. In all cases, intensity is color coded on a 40 dB scale.

$$\int_{-\infty}^{\infty} \exp(-px^2 + qx)\mathrm{d}x = \sqrt{\frac{\pi}{p}} \exp\left(\frac{q^2}{4p}\right). \quad \textbf{(15)}$$

Using $E(x, y, z) = A_0 F(x, y, z)e^{i\phi}$, we can write $F(x, y, z)$ in the form

$$F(x, y, z) = \frac{w_0}{w(z)} \exp\left(-\frac{x^2 + y^2}{2w^2(z)}\right). \quad \textbf{(16)}$$

The preceding result shows that a Gaussian beam retains its shape inside the GRIN fiber but its width $w(z)$ oscillates in a periodic manner as

$$w(z) = w_0\sqrt{f(z)}, \quad f(z) = \cos^2(\pi z/z_p) + C^2 \sin^2(\pi z/z_p), \quad \textbf{(17)}$$

where the parameter C is defined as

$$C = \frac{z_p}{\beta S}, \quad S = \pi w_0^2. \quad \textbf{(18)}$$

Here, S is the beam's cross-sectional area. Over one self-imaging period z_p, the beam width first decreases from w_0 to $w_0 C$ at the mid-point and then recovers its input value at the end of the period. Figure 1(a) shows how the Gaussian beam evolves inside the fiber by plotting the intensity $|F(x, y, z)|^2$ over two self-imaging periods for $C = 0.2$. As seen there, the beam is compressed by a factor of five at the midpoint of each period. The effective beam area can be calculated analytically by substituting $F(x, y, z)$ into Eq. (13). The result is found to be $A_{\text{eff}}(z) = A_{\text{eff}}(0) f(z)$, with $A_{\text{eff}}(0) = 2\pi w_0^2$.

B. Circular Beam

Next we consider an input beam with constant intensity over a circular region. In cylindrical coordinates, the input field can be written as

$$E(\rho', \phi', 0) = \begin{cases} A_0 & \text{if } \rho' \leq \rho_0 \\ 0 & \text{otherwise,} \end{cases} \qquad \textbf{(19)}$$

where ρ_0 is the radius of the circular beam. The field at a distance z is found by writing Eq. (5) in the cylindrical coordinates as follows:

$$E(\rho, \phi, z) = \int_0^\infty \int_0^{2\pi} K(\rho, \rho'; \phi, \phi') E(\rho', \phi', 0) \rho' d\phi' d\rho', \qquad \textbf{(20)}$$

where the kernel $K(\rho, \rho'; \phi, \phi')$ takes the form

$$K(\rho, \rho'; \phi, \phi') \frac{\beta}{2\pi i} \left(\frac{b}{\sin(bz)} \right) e^{i\beta z}$$

$$\times \exp\left[\frac{i}{2}\beta b \cot(bz)(\rho^2 + \rho'^2) - \frac{i\beta b \rho \rho'}{\sin(bz)} \cos(\phi - \phi') \right]. \qquad \textbf{(21)}$$

As $E(\rho', \phi', 0)$ does not depend on ϕ', the integration over ϕ' in Eq. (20) can be done using the result

$$\int_0^{2\pi} \exp\left[-ip \cos(\phi - \phi') \right] d\phi' = 2\pi J_0(p), \qquad \textbf{(22)}$$

where J_0 is the zero-order Bessel function. The integration over ρ' must be done numerically. Using $r = \rho/\rho_0$, this integral takes the form

$$E(r, \phi, z) = \frac{A_0 e^{i\beta z}}{iC \sin(\pi z/z_p)} \exp\left[\frac{ir^2}{2C} \cot(\pi z/z_p) \right]$$

$$\int_0^1 r' J_0\left(\frac{rr'}{C \sin(\pi z/z_p)} \right) \exp\left[\frac{ir'^2}{2C} \cot(\pi z/z_p) \right] dr', \qquad \textbf{(23)}$$

where the parameter C is as defined as in Eq. (18) with $S = \pi \rho_0^2$. As expected, the field does not depend on ϕ, indicating that the circular symmetry is preserved during the beam propagation. Figure 1(c) shows how the circular beam evolves over two self-imaging periods using $C = 0.1$. Note the fringe-like structure appearing as the beam is compressed because of diffraction. The effective beam area is found by doing the double integral in Eq. (12) to obtain

$$A_{\text{eff}}(0) = \pi \rho_0^2, \quad f(\xi) = \frac{2 \left(\int_0^\infty r|F(r, \xi)|^2 dr \right)^2}{\left(\int_0^\infty r|F(r, \xi)|^4 dr \right)}. \qquad \textbf{(24)}$$

C. Square-Shaped Beam

As a third example, we consider the case of an input beam with constant intensity over a square region. The input field in this case is of the form

$$E(x', y', 0) = \begin{cases} A_0 & \text{if } |x'| \leq \frac{1}{2}l_0 \text{ and } |y'| \leq \frac{1}{2}l_0 \\ 0 & \text{otherwise,} \end{cases} \qquad \textbf{(25)}$$

where l_0 represents the length of each side. On substituting this form into Eq. (5), the field at a distance z can be expressed as

$$E(x, y, z) = \frac{A_0 e^{i\psi}}{2iC \sin(\pi z/z_p)} V(x/l_0, z/z_p) V(y/l_0, z/z_p), \qquad \textbf{(26)}$$

where the function $V(X, Z)$ is defined as

$$V(X, Z) = \int_{-\frac{1}{2}}^{\frac{1}{2}} \exp\left[\frac{\pi i}{2C \sin(\pi Z)} (\cos(\pi Z) X'^2 - 2XX') \right] dX'. \qquad \textbf{(27)}$$

Figure 1(c) shows how the square-shaped beam evolves over two self-imaging periods for $C = 0.1$ by calculating this integral numerically. Similar to the case of a circular beam, a large number of fringes appear because of diffraction as the beam is compressed. The function $f(z)$ is calculated by doing the double integral in Eq. (12) numerically and using the relation $A_{\text{eff}}(0) = l_0^2$.

D. Off-Centered Gaussian Beam

When an input beam is launched into a GRIN fiber such that its center coincides with the fiber's axis, only radially symmetric modes of the GRIN fiber are excited in view of the circular symmetry. All three beam shapes considered so far fall into this category. When the beam center is shifted from the fiber's axis, the radial symmetry is broken and many more modes are often excited. Indeed, an off-centered input beam has been launched intentionally in some experiments [19]. Even when an on-center launch is desirable, it may be difficult to realize it.

For the simplicity of the following discussion, we consider an off-centered Gaussian beam and assume that its center is shifted from the fiber's axis by an amount x_0 along the x axis. The input beam field in this case is given by

$$E(x', y', 0) = A_0 \exp\left(-[(x' - x_0)^2 + y'^2]/(2w_0^2) \right). \qquad \textbf{(28)}$$

The propagated field is found by following the same procedure used in the case of the centered Gaussian beam. Both integrals in Eq. (5) can still be done analytically using the result given in Eq. (15). The spatial distribution $F(x, y, z)$ in Eq. (12) is modified for the shifted beam and is given by

$$F(x, y, z) = \frac{w_0}{w(z)} \exp\left(-\frac{[x - x_0 \cos(\pi z/z_p)]^2 + y^2}{2w^2(z)} \right), \qquad \textbf{(29)}$$

where the beam width $w(z)$ is the same as in Eq. (17). Figure 1(b) shows how the off-centered Gaussian beam evolves over two self-imaging periods using $x_0 = w_0$ and $C = 0.2$. The new feature is that the beam shifts its center as its width is reduced in such a way that after a distance of z_p, it is centered on the opposite side at $x = -x_0$. After that, the beam moves to the right side to recover its original position at a distance of $2z_p$. In essence, the beam propagates in a zigzag manner, as seen in Fig. 1(b). This doubling of the self-imaging period is a consequence of the broken circular symmetry of an off-axis input beam, The self-imaging theory in Section 2 predicts this behavior, where it is found that the self-imaging period is indeed $2z_p$ for such beams.

4. IMPACT ON THE NONLINEAR EFFECTS

As seen from the effective NLS equation in Eq. (11), the effect of spatial changes in the beam shape appear through the periodic oscillations of the nonlinear parameter along the length of a GRIN fiber. Periodic compression of optical beams reduces the effective beam area in the middle of each self-imaging period, which enhances the nonlinear effects through a larger value $\bar{\gamma}(z)$. Equation (12) shows that this periodic enhancement is governed by a dimensionless function $f^{-1}(z)$. This provides a simple way to study the impact of input beam shape on the nonlinear evolution of pulsed optical beams inside a GRIN fiber.

Figure 2 shows how $f^{-1}(z)$ varies over one self-imaging period for the three beam shapes considered in Section 3. The dashed curve for the Gaussian beam for a specific value $C = 0.2$ is relatively smooth and peaks in the middle, where the beam is compressed most, resulting in the smallest beam area. A similar behavior occurs for the beams with constant intensity over circular and square regions with two main differences, both related to the diffraction properties of such beams. First, the amplitude of the central peak is reduced considerably. Second, an oscillatory structure appears near the beginning and the end of each period. The origin of these oscillations is related to the fringe-like diffraction pattern seen in Figs. 1(c) and 1(d). In the case of an off-axis Gaussian beam, the function $f(z)$ is found to be identical to that of the on-axis Gaussian beam, suggesting that the periodic movement of the beam center around the fiber's axis does not affect any nonlinear effect. This appears somewhat surprising but can be understood by noting that the effective beam area and its variations along the z axis are not affected by movement of the beam center, as long as the initial shift x_0 of the beam center is small enough that the entire Gaussian beam remains confined within the fiber's core.

The results in Fig. 2 indicate that the beam shape will affect all nonlinear effects whose behavior is governed by the effective NLS equation in Eq. (11). To study the shape-induced changes, we need to solve Eq. (11) numerically. In order to compare the nonlinear effects for different beam shapes, we must ensure that the initial value of γ at the input end is the same for all beams, i.e., all beams should have not only the same optical power
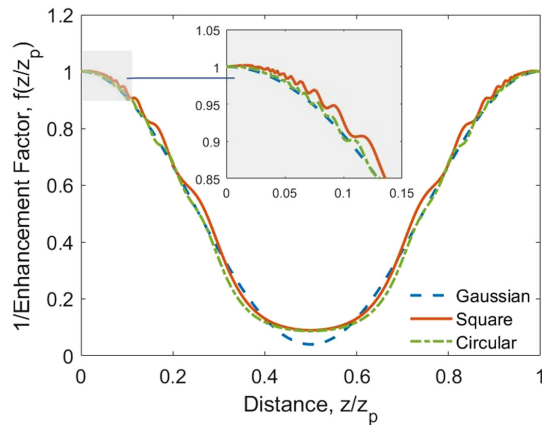
but also the same initial effective area $A_{\text{eff}}(0)$. This area can be calculated analytically for the Gaussian beam and is given by $A_{\text{eff}}(0) = 2\pi w_0^2$. Its value is $\pi \rho_0^2$ for the circular beam and l_0^2 for the square beam. The same value $A_{\text{eff}}(0)$ is ensured by choosing the aperture-size parameters such that $\rho_0 = \sqrt{2}w_0$ and $l_0 = \sqrt{2\pi}\,w_0$. We stress that physical beam area S is not the same in this situation. It is easy to show that $S = \pi w_0^2$ for the Gaussian beam, but it equals $2\pi w_0^2$ for the circular and square beams. As a result, the C parameter given in Eq. (18) is doubled for the Gaussian beam, compared to that of the circular and square beams.

A. Impact on Modulation Instability

We first explore how different input beam shapes affect the phenomenon of modulation instability, also known as GPI and studied since 2003 in the context of a Gaussian input beam [4,5]. It was found that GPI can produce a large number of sidebands on both sides of the pump frequency even when a CW Gaussian beam is launched in the normal-GVD region of a GRIN fiber. The physical origin of these sidebands lies in the periodic nature of the nonlinear parameter. The CW solution to Eq. (11) is perturbed using

$$A(z, t) = (\sqrt{P_0} + a)\exp\left(i\gamma P_0 \int_0^z f^{-1}(z')\mathrm{d}z'\right), \quad \textbf{(30)}$$

where P_0 is the input power and $a(z, t)$ represents a small perturbation. Linearizing Eq. (11) in terms of $a(z, t)$, we obtain

$$\frac{\partial a}{\partial z} + i\frac{\beta_2}{2}\frac{\partial^2 a}{\partial t^2} = i\gamma P_0 f^{-1}(z)(a + a^*). \quad \textbf{(31)}$$

This equation can be solved in the frequency domain by assuming $a(z, t) = a_1 e^{i\Omega t} + a_2 e^{-i\Omega t}$ and expanding the enhancement factor in a Fourier series as $f^{-1}(z) = \sum c_m \exp(im2\pi z/z_p)$. Following the analysis given in Ref. [27], one finds that the phase matching provided by the nonlinear Kerr grating (formed through self-imaging) leads to an infinite number of sideband pairs at frequencies shifted from ω_0 by

$$\Omega_m = \pm\left(\frac{2\pi m}{\beta_2 z_p} - \frac{2c_0}{\beta_2 L_{NL}}\right)^{1/2}, \quad \textbf{(32)}$$

where $L_{NL} = 1/(\gamma P_0)$ is the nonlinear length, and the integer m can take both positive and negative values. As the self-imaging period ($z_p < 1$ mm) is much shorter than L_{NL} in practice, sidebands form for positive values of m in the case of normal GVD ($\beta_2 > 0$). In contrast, when $\beta_2 < 0$, sidebands form for $m = 0$ and for negative values of m. The amplitude of the mth-order sidebands grows from noise as $e^{g_m z}$, where the gain g_m depends on the magnitude c_m of the Fourier coefficient [27].

The important question is how the amplitudes and frequencies of the GPI sidebands are affected when the beam shape is not Gaussian. It should be clear that the Fourier coefficient c_m will change for different beam shapes because the function $f(z)$ changes for them (see Fig. 2). Table 1 lists the value of c_m for $m = 0$ to 4 for the Gaussian, circular, and square beam shapes considered in Section 3. As seen from Eq. (32), the sideband frequencies depend only on the coefficient c_0.


Fig. 2. Variation of the enhancement factor f^{-1} over one self-imaging period for the three beams considered in Section 3. The inset clearly reveals the oscillatory structure in the case of circular and square-shaped beams.

Table 1.　Values of Several Fourier Coefficients Associated with the Three Beams Discussed in Section 3

	$|c_0|$	$|c_1|$	$|c_2|$	$|c_3|$	$|c_4|$
Gaussian	5.0000	3.3333	2.2222	1.4815	0.9877
Circular	4.0573	2.3321	1.1096	0.3502	0.0030
Square	3.7669	2.1457	1.0904	0.4181	0.0725

In the case of anomalous GVD, the frequencies of the $m = 0$ sidebands scale as $\sqrt{c_0}$, and, thus, they will be different for the three beam shapes. This sideband pair does not form in the case of normal GVD. As the first term in Eq. (32) dominates in this situation, the sideband frequencies are not affected much by the beam shape for $m \neq 0$. However, the amplitudes of all sidebands depend on the beam shape through the magnitude of the Fourier coefficients c_m, irrespective of whether the GVD is normal or anomalous at the pump wavelength.

To verify that the sideband amplitudes are indeed different for different beam shapes, we consider the propagation of a CW pump beam at 1064 nm with a peak power of 50 kW inside a GRIN fiber with a core refractive index $n_1 = 1.47$ and a self-imaging period $z_p = 0.615$ mm. The GVD parameter is $\beta_2 = 20$ ps^2/km. For the Gaussian beam, we choose $C = 0.2$ and determine the corresponding spot size as $w_0 = 10.6$ µm. The circular and square beams with the same initial effective area have a radius of $\rho_0 = 15$ µm and side length of $l_0 = 26.6$ µm, respectively. At $z = 0$, the nonlinear parameter $\bar{\gamma} = 0.267$ W^{-1}/km is the same for all three beam shapes considered. The nonlinear length for these parameters is only 7.5 cm. We solve Eq. (11) numerically with a fourth-order Runge–Kutta method in the interaction picture [26]. Following Ref. [24], to seed the sideband formation, we add a narrow temporal spike (width 1 fs) with a peak power equal to one-tenth of the CW pump power. The function $f(z)$ calculated in Section 3 is used for three different beam shapes. Figure 3 compares the output spectrum at a distance of 15 cm for the (a) Gaussian, (b) circular, and (c) square-shaped beams.

Several things are noteworthy in Fig. 3. First, the frequencies of the spectral sidebands are the same for all three beam shapes.
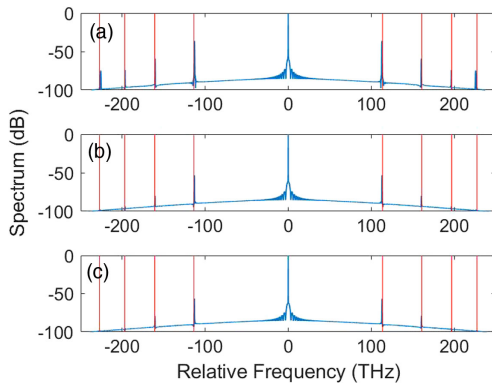
Fig. 3. Comparison of GPI sidebands after 15 cm of propagation for (a) Gaussian, (b) circular, and (c) square-shaped beams. In each case, the CW peak power is 50 kW, and the beam size is chosen such that the effective beam area $A_{\text{eff}}(0)$ is the same. The red lines show the frequencies predicted by Eq. (32).

This is expected since the term containing the Fourier coefficient c_0 in Eq. (32) is negligible for $m \neq 0$. We have verified that the frequency of the $m = 0$ sideband forming in the case of $\beta_2 < 0$ indeed is different for different beam shapes. Second, the sideband amplitudes in Fig. 3 change considerably for different beam shapes. This is understood by noting that the sidebands grow from the initial seed as $a_m(z) = a_m(0) \exp(g_m z)$, where the gain coefficient g_m depends on the Fourier coefficient c_m as $g_m = 2\gamma P_0 |c_m|$ [27]. Since c_m's are the largest for a Gaussian beam in Table 1, the sideband amplitudes are the largest for this beam. Indeed, the amplitude ratios in Fig. 3 agree quite well with the ratio expected by comparing the c_m coefficients for different beam shapes. The main point to note is that although there are quantitative differences in the amplitudes of the GPI sidebands, the overall spectral features are remarkably similar for all beam shapes.

B. Evolution of Higher-Order Solitons

When a short optical pulse propagates in the anomalous-GVD region of a GRIN fiber, it forms a high-order soliton, whose evolution is significantly affected by the nonlinear index grating created by the spatial self-imaging [17–19]. In particular, this grating creates multiple dispersive waves at specific frequencies governed by a phase-matching condition [16]. Similar to the case of GPI, one expects that the temporal and spectral evolution of a high-order soliton would be affected considerably by the beam shape. To study this impact, we first extend Eq. (11) to include the higher-order effects resulting from third-order dispersion (TOD) and intrapulse Raman scattering [26]:

$$\frac{\partial A}{\partial z} + i\frac{\beta_2}{2}\frac{\partial^2 A}{\partial t^2} + \frac{\beta_3}{6}\frac{\partial^3 A}{\partial t^3} = i\gamma f^{-1}(z)$$

$$\times A(z,t) \int_0^\infty R(t')|A(z, t-t')|^2 \mathrm{d}t', \qquad \textbf{(33)}$$

where $R(t) = (1 - f_R)\delta(t) + f_R h_R(t)$, with $f_R = 0.18$. Here, β_3 accounts for the TOD effects, and the Raman response function $h_R(t)$ includes intrapulse Raman scattering.

We solve this equation numerically assuming that a pulsed beam at a wavelength of 1550 nm is launched into the same GRIN fiber used for Fig. 3. At this wavelength, the GVD and TOD parameters have values $\beta_2 = -22$ ps^2/km and $\beta_3 = 1.32 \times 10^{-1}$ ps^3/km. Once again, we set the C parameter of the Gaussian beam as $C = 0.2$ and determine the spot size and radius of the Gaussian and circular beams, respectively, such that both beams have the same initial effective area. The top and bottom rows in Fig. 4 compare the temporal and spectral features for the Gaussian and circular beams, respectively, at a distance of 10 cm. The initial amplitude of the input pulse is taken to be $A(0, t) = \sqrt{P_0}\mathrm{sech}(t/T_0)$, with $T_0 = 30$ fs, which corresponds to a full width at half maximum of about 53 fs. The peak power is chosen such that the soliton order, $N = \gamma P_0 T_0^2/|\beta_2|$, has a value of two [26].

Figure 4 shows most of the temporal and spectral features expected for a second-order soliton even inside a single-mode fiber. The soliton undergoes fission at a distance of about 1 cm, forming first-order solitons whose spectra shift toward the red side through intrapulse Raman scattering. Whereas a single
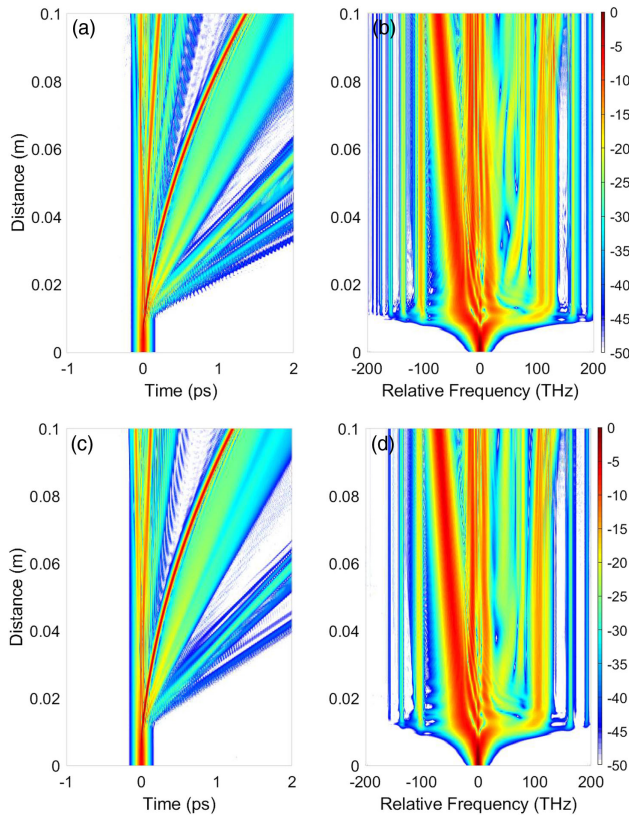
Fig. 4. (a) Temporal and (b) spectral evolution patterns over a distance of 10 cm for a second-order soliton propagating inside a GRIN fiber as a Gaussian beam. (c), (d) Comparison of the evolution patterns for a circular beam. In all cases, intensity is color coded on a 50 dB scale.

dispersive wave is generated in the case of a single-mode fiber, the nonlinear index grating resulting from spatial self-imaging of the beam creates multiple dispersive waves in the case of a GRIN fiber. The frequency of these waves is governed by a phase-matching condition of the form [24]

$$\frac{\beta_2}{2}\Omega^2 + \frac{\beta_3}{6}\Omega^3 - \delta\beta_1\Omega = \frac{2\pi m}{z_p} + \frac{c_0 \gamma P_1}{2}, \quad (34)$$

where P_1 is the peak power of the shortest soliton formed after the fission process, and $\delta\beta_1$ accounts for changes in the group velocity of the soliton from its inital value. The first term on the right side results from the nonlinear index grating, and it contains m that can take any integer value. The choice of $m = 0$ corresponds to the single dispersive wave formed inside a single-mode fiber. Solutions to Eq. (34) for $m \neq 0$ provide frequencies of dispersive waves formed only in GRIN fiber and whose formation depends to some extent on the spatial shape of the beam.

A comparison of the top and bottom rows in Fig. 4 shows again that although quantitative differences exist, most qualitative features are independent of a specific beam shape. We estimated $\delta\beta_1$ from the slope of the tilted soliton in Fig. 4 and used Eq. (34) to calculate the frequency of the dispersive waves for $m = 0$. The calculated values were 112 THz and 109 THz for the Gaussian and circular-shaped beams, respectively. These values agree to within 0.5% with the corresponding spectral

peaks in Fig. 4. Another quantitative difference is that the dispersive waves formed for $m \neq 0$ in Eq. (34) are less intense in the case of a circular beam compared to a Gaussian beam. The frequencies of these waves are also slightly different because of the presence of c_0 in Eq. (34). However, this difference is too small to be noticeable in Fig. 4 because the first term on the right side of Eq. (34) dominates in practice. Another difference is that the Raman-induced spectral shift is larger in the case of the pulsed Gaussian beam. We have not shown the case of a square-shaped beam because its evolution is almost identical to that of a circular beam. This is so because we have chosen beam sizes such that the effective beam areas are the same for both beams.

We briefly discuss the impact of higher-order dispersion terms. We carried out numerical simulations by including the fourth-order dispersion term using $\beta_4 = -1.90 \times 10^{-4}\,\text{ps}^4/\text{km}$. As is well known from past work [28], an additional dispersive wave can form in this situation even in the absence of self-imaging. We observed such a wave but its amplitude was relatively small. Although sideband frequencies shift slightly when fourth-order dispersion is included, the overall qualitative behavior is not affected significantly.

5. EFFECTS OF PHASE-FRONT CURVATURE

It has been assumed implicitly so far that the optical beam has a plane phase front at the input end of the fiber located at $z = 0$. This may not always be the case in practice. In fact, the curvature of the phase front has been tailored in some experiments to control and optimize a specific nonlinear process [29,30]. As an example, we consider an input Gaussian beam whose phase front is curved such that the spatial phase varies in a parabolic fashion in the transverse plane. The input field for such a Gaussian beam can be written as

$$E(x', y', 0) = A_0 \exp\left(-\frac{(1 + i S_c)(x'^2 + y'^2)}{2w_0^2}\right), \quad (35)$$

where S_c controls the phase-front curvature. Here, we refer to S_c as the spatial chirp parameter, in analogy with the temporal chirp of pulses having a parabolic phase profile.

We can study the spatial evolution of such a Gaussian wave using the self-imaging theory in Section 2. This requires performing integrations over x' and y' after substituting $E(x', y', 0)$ from Eq. (35) into Eq. (5). The process is similar to that carried out in Section 3.A for a Gaussian beam with $S_c = 0$. After considerable algebra, we find that the spatial distribution $F(x, y, z)$ has the same functional form as in Eq. (16) with the beam width oscillating as $w(z) = w_0\sqrt{f(z)}$, but the functional form of $f(z)$ is modified as

$$f(z) = [\cos(\pi z/z_p) - S_c C \sin(\pi z/z_p)]^2 + C^2 \sin^2(\pi z/z_p). \quad (36)$$

As expected, we recover the result given in Eq. (17) for $S_c = 0$ corresponding to a Gaussian beam with no phase-front curvature.

The function $f(z)$ given in Eq. (36) has several novel features introduced by the spatial chirp S_c. Notice first that $f(z) = 1$ at $z = mz_p$, where m is any integer, indicating that the periodicity of spatial oscillations is not affected by the spatial chirp.
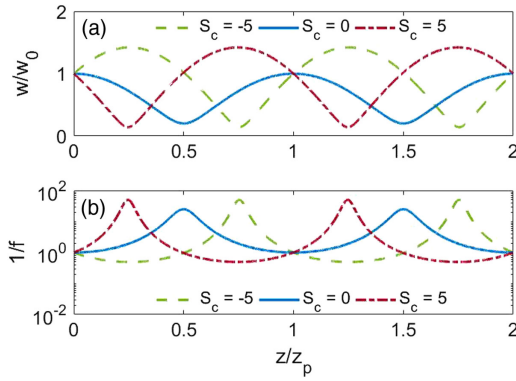
Fig. 5. (a) Beam-width oscillations of spatially chirped Gaussian beams over two self-imaging periods for $S_c = -5$, 0, 5 with $C = 0.2$. (b) Corresponding nonlinear enhancement $f^{-1}(z)$ over the same distance shown on a logarithmic scale.

Fig. 6. Comparison of optical spectra at a distance of 10 cm for (a) $S_c = -5$, (b) $S_c = 0$, and (c) $S_c = 5$. A pulsed Gaussian beam with a curved phase front is launched into the GRIN fiber when $S_c \neq 0$.

However, the nature of beam-width oscillation changes considerably with S_c. Figure 5(a) shows how the beam width oscillates over two periods for $S_c = \pm 5$; the case of $S_c = 0$ is also shown for comparison. The major change induced by the spatial chirp is that the minimum beam width no longer occurs in the middle of each period. For a positive value of S_c, the minimum value occurs before the midpoint and is smaller than the $S_c = 0$ case. However, the beam expands after this minimum, and the beam width becomes larger than the initial width over a considerable part of the period. The exact opposite occurs for a negative value of S_c. Now, the beam expands during the first half of the cycle, and the beam width becomes larger than the initial width over a considerable part of the cycle. The minimum value occurs after the midpoint during the compression phase.

As one would expect, changes in the beam width translate into changes in the effective beam area through $A_{\text{eff}}(z) = 2\pi w^2(z) = A_{\text{eff}}(0) f^{-1}(z)$, i.e., the inverse function $f^{-1}(z)$ controls the nonlinear enhancement. Figure 5(b) shows the enhancement of the nonlinear parameter γ over two self-imaging periods for $S_c = \pm 5$; the case of $S_c = 0$ is also shown for comparison. As expected, the enhancement factor is larger compared to the unchirped case at the point of maximum beam compression, but it also becomes less than one over a considerable portion of the cycle as the beam expands.

It is not clear from these results to what extent the phase-front curvature is helpful in enhancing the nonlinear effects. We use numerical simulations to examine this issue further. We use the same simulation parameters used for Fig. 4 but consider the case of a pulsed Gaussian beam with a curved phase front by varying the value of S_c. Figure 6 compares the output spectra at a distance of 10 cm for values of $S_c = -5$, 0, and 5. The spectra look quite similar, but a closer inspection reveals that the dispersive waves emitted on the red side of the input spectrum are enhanced when the phase front of the Gaussian beam is curved. This asymmetry has its origin in the asymmetric evolution of the beam width within a self-imaging period seen in Fig. 5. Mathematically speaking, the enhancement factor $f^{-1}(z)$ does not remain an even function around the mid-point $z_p/2$. It is this symmetry breaking that leads to spectral asymmetry in both the formation of GPI sidebands and generation of dispersive waves.
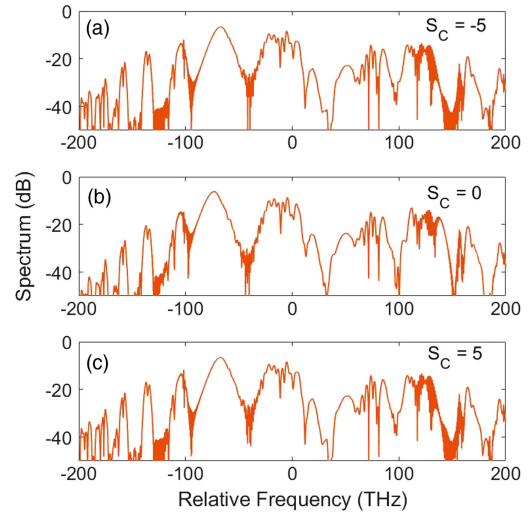
For a comprehensive treatment, we also consider a circular-shaped input beam with phase-front curvature. The input field then takes the form

$$E(\rho', \phi', 0) = \begin{cases} A_0 \exp\left(-\frac{i S_c \rho'^2}{\rho_0^2}\right) & \text{if } \rho' \leq \rho_0 \\ 0 & \text{otherwise.} \end{cases} \quad (37)$$

Note from the relationship $\rho_0 = \sqrt{2} w_0$ established earlier, the phase-front curvature of the circular-shaped beam is equivalent to that considered in the Gaussian case. Following the procedure outlined in Section 3.B, we find that the spatial evolution of the chirped circular beam is described by

$$E(r, \phi, z) = \frac{A_0 e^{i\beta z}}{i C \sin(\pi z/z_p)} \exp\left[\frac{ir^2}{2C} \cot(\pi z/z_p)\right]$$

$$\times \int_0^1 r' J_0\left(\frac{rr'}{C \sin(\pi z/z_p)}\right)$$

$$\times \exp\left[ir'^2\left(\frac{\cot(\pi z/z_p)}{2C} - S_c\right)\right] dr', \quad (38)$$

which reverts back to Eq. (23) when $S_c = 0$. Figure 7 shows how our choice of the spatial chirp parameter $S_c = -5$, 0, 5 impacts the enhancement factor $f^{-1}(z)$ of the nonlinear parameter γ over one self-imaging period. Qualitatively, we observe the same behavior as in the case of the chirped Gaussian pulse. Introduction of the spatial chirp breaks up the symmetry of the enhancement factor $f^{-1}(z)$ over each self-imaging period. In the case of $S_c = 5$, it peaks before the midpoint and then remains below one over a significant part of the period. This behavior is reversed in the case of negative S_c. We carried out a numerical simulation to study the impact of the spatial chirp on beam propagation. Once again we use the same simulation parameters used for Fig. 4 and propagate over a distance of 10 cm. By comparing the output spectra for $S_c = -5$ and 5 against that of $S_c = 0$, we note that similar to the case of the chirped Gaussian pulse, the dispersive waves generated on the
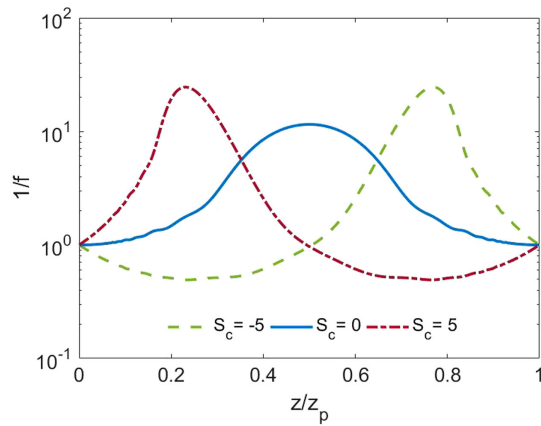
Fig. 7. Nonlinear enhancement factor $f^{-1}(z)$ of spatially chirped circular-shaped beams over one self-imaging period for $S_c = -5$, 0, and 5 with $C = 0.1$. Results shown on a logarithmic scale.

Fig. 8. (a) Temporal and (b) spectral evolution of a pulsed circular beam over a distance of 5 cm inside a GRIN fiber using the 4D numerical model with input parameters identical to those used in Figs. 4(c) and 4(d).

red side of the input spectrum experience greater enhancement when the phase front of the circular-shaped beam is curved. This can be attributed to the asymmetric nature of the enhancement factor over each self-imaging period. Given the observation of similar spectral features as in Fig. 6, we have chosen not to show the output spectra of the spatially chirped circular beams.

6. DISCUSSION AND CONCLUSION

In this paper, we have used the well-known periodic self-imaging of optical beams inside a GRIN fiber to study the impact of spatial shape and phase-front curvature on the temporal and spectral evolutions of optical pulses inside the fiber. The main assumption used in our work is that an effective NLS equation [24], containing a periodically oscillating nonlinear parameter $\gamma(z)$, includes all spatial effects, but the spatial evolution is not affected by temporal dynamics of the pulse. This clearly cannot be valid under all conditions, but a domain of input parameters exists where this assumption has been found to be a reasonable one.

To ensure that our input parameter lies in the regime where the simple NLS equation used in this work can be applied, we solved numerically the four-dimensional (4D) equation given in Eq. (10) for the case in which a circular beam (constant intensity over a circular region) is launched into the GRIN fiber. The power $P(z, t)$ was calculated by integrating $|E|^2$ over the beam cross section. The results are shown in Fig. 8, where we show the temporal and spectral evolutions of the pulsed beam. This figure should be compared with Figs. 4(c) and 4(d) for which the 2D NLS equation was used with the identical input parameters (except that the evolution is shown over 10 cm). It is hard to notice any visible differences because the simpler model captures all temporal and spectral features reasonably accurately.

To reveal the quantitative differences, we compare in Fig. 9 the optical spectra at a distance of 5 cm for the 2D and 4D numerical simulations in the case of a pulsed circular-shaped beam with all identical input parameters. It is evident that almost all qualitative features are produced by the simpler 2D model, although some quantitative differences do remain. For example, note that the amplitudes of the dispersive waves are
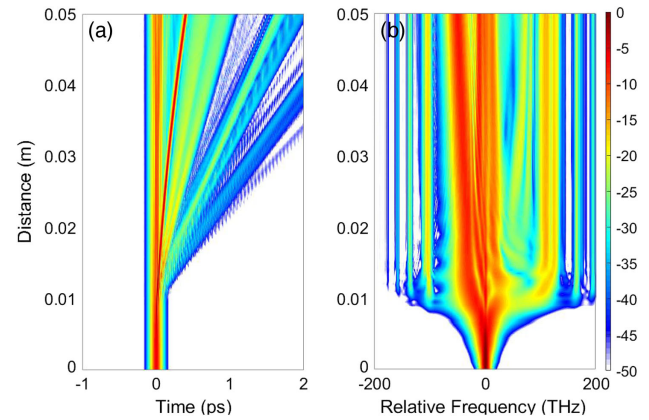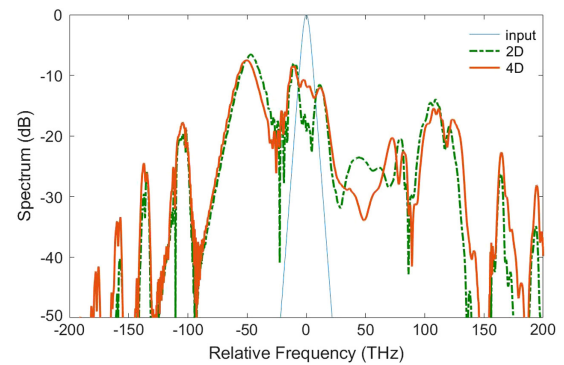
Fig. 9. Comparison of output spectra at a distance of 5 cm for the 2D and 4D numerical simulations in the case of a pulsed circular-shaped beam with all identical input parameters. The thin blue line represents the input spectral profile.

larger in the 4D simulation compared to those in the 2D case. This could be a real effect but may also be related to the spatial resolution used in the 4D simulations. Even though these simulations took more than 24 h on a modern laptop, the spatial grid in the x and y directions had only 128 points. Nevertheless, the results shown in Fig. 9 show that the 2D model is capable of capturing most of the temporal and spectral features when pulsed beams containing a train of femtosecond pulses evolve inside GRIN fibers under the influence of Kerr and Raman nonlinearities.

In conclusion, we have presented a general framework capable of describing the nonlinear propagation of pulsed optical beams of arbitrary shapes and phase fronts inside a GRIN fiber. The main assumption made is that the spatial self-imaging features of the beam are not affected by the temporal evolution of optical pulses. A propagation kernel known from the work done in the 1970s is used to obtain a distance-dependent nonlinear coefficient that captures all spatial effects within an effective 2D NLS equation. We have considered three beam shapes (Gaussian, circular, and square) to study the impact of the shape, position, and curvature of optical beams on the

complex spatiotemporal dynamics specific to GRIN fibers. In particular, we focused on the effects of input beam shape on the creation of GPI sidebands and the generation multiple dispersive waves when higher-order solitons form and propagate inside a GRIN fiber. The results of our numerical analysis indicate that for beam widths chosen to yield the same value of the effective mode area at the input end of the fiber, the nonlinear effects are pronounced considerably when a Gaussian beam is launched into the fiber. We also found that even though the self-imaging period is doubled when an off-centered Gaussian beam is launched into a GRIN fiber, it does not affect the nonlinear evolution because the effective beam area still maintains the same periodicity, as long as the shift in the beam's center is not so large that it does not remain confined to the fiber's core.

REFERENCES

1. A. Mafi, "Pulse propagation in a short nonlinear graded-index multimode optical fiber," J. Lightw. Technol. **30**, 2803–2811 (2012).
2. K. Krupa, V. Couderc, A. Tonello, A. Picozzi, A. Barthélémy, G. Millot, and S. Wabnitz, "Spatiotemporal nonlinear dynamics in multimode fibers," in *Nonlinear Guided Wave Optics*, S. Wabnitz, ed. (IOP Science, 2017), Chap. 14.
3. G. P. Agrawal, "Self-imaging in multimode graded-index fibers and its impact on the nonlinear phenomena," Opt. Fiber Technol. **50**, 309–316 (2019).
4. S. Longhi, "Modulational instability and space-time dynamics in nonlinear parabolic-index optical fibers," Opt. Lett. **28**, 2363–2365 (2003).
5. K. Krupa, A. Tonello, A. Barthélémy, V. Couderc, B. M. Shalaby, A. Bendahmane, G. Millot, and S. Wabnitz, "Observation of geometric parametric instability induced by the periodic spatial self-imaging of multimode waves," Phys. Rev. Lett. **116**, 183901 (2016).
6. R. Chang and J. Wang, "Optical soliton in graded-index waveguides," Opt. Lett. **18**, 266–268 (1993).
7. S. S. Yu, C. H. Chien, Y. Lai, and J. Wang, "Spatio-temporal solitary pulses in graded-index materials with Kerr nonlinearity," Opt. Commun. **119**, 167–170 (1995).
8. S. Raghavan and G. P. Agrawal, "Spatiotemporal solitons in inhomogeneous nonlinear media," Opt. Commun. **180**, 377–382 (2000).
9. W. H. Renninger and F. W. Wise, "Optical solitons in graded-index multimode fibre," Nat. Commun. **4**, 1719 (2013).
10. Z. Zhu, L. G. Wright, D. N. Christodoulides, and F. W. Wise, "Observation of multimode solitons in few-mode fiber," Opt. Lett. **41**, 4819–4822 (2016).
11. A. S. Ahsan and G. P. Agrawal, "Graded-index solitons in multimode fibers," Opt. Lett. **43**, 3345–3348 (2018).
12. Z. Liu, L. G. Wright, D. N. Christodoulides, and F. W. Wise, "Kerr self-cleaning of femtosecond-pulsed beams in graded-index multimode fiber," Opt. Lett. **41**, 3675–3678 (2016).
13. K. Krupa, A. Tonello, B. M. Shalaby, M. Fabert, A. Barthélémy, G. Millot, S. Wabnitz, and V. Couderc, "Spatial beam self-cleaning in multimode fibres," Nat. Photonics **11**, 237–241 (2017).
14. E. Deliancourt, M. Fabert, A. Tonello, K. Krupa, A. Desfarges-Berthelemot, V. Kermene, G. Millot, A. Barthélémy, S. Wabnitz, and V. Couderc, "Kerr beam self-cleaning on the mode in graded-index multimode fibers," OSA Continuum **2**, 1089–1096 (2019).
15. K. Krupa, G. G. Castañeda, A. Tonello, A. Niang, D. S. Kharenko, M. Fabert, V. Couderc, G. Millot, U. Minoni, D. Modotto, and S. Wabnitz, "Nonlinear polarization dynamics of Kerr beam self-cleaning in a graded-index multimode optical fiber," Opt. Lett. **44**, 171–174 (2019).
16. L. G. Wright, D. N. Christodoulides, and F. W. Wise, "Controllable spatiotemporal nonlinear effects in multimode fibre," Nat. Photonics **9**, 306–310 (2015).
17. K. Krupa, C. Louot, V. Couderc, M. Fabert, R. Guenard, B. M. Shalaby, A. Tonello, D. Pagnoux, P. Leproux, A. Bendahmane, R. Dupiol, G. Millot, and S. Wabnitz, "Spatiotemporal characterization of supercontinuum extending from the visible to the mid-infrared in a multimode graded-index optical fiber," Opt. Lett. **41**, 5785–5788 (2016).
18. G. Lopez-Galmiche, Z. Sanjabi Eznaveh, M. A. Eftekhar, J. Antonio Lopez, L. G. Wright, F. Wise, D. Christodoulides, and R. Amezcua Correa, "Visible supercontinuum generation in a graded index multimode fiber pumped at 1064 nm," Opt. Lett. **41**, 2553–2556 (2016).
19. M. A. Eftekhar, L. G. Wright, M. S. Mills, M. Kolesik, R. Amezcua Correa, F. W. Wise, and D. N. Christodoulides, "Versatile supercontinuum generation in parabolic multimode optical fibers," Opt. Express **25**, 9078–9087 (2017).
20. M. Karlsson, D. Anderson, and M. Desaix, "Dynamics of self-focusing and self-phase modulation in a parabolic index optical fiber," Opt. Lett. **17**, 22–24 (1992).
21. G. P. Agrawal, A. K. Ghatak, and C. L. Mehta, "Propagation of a partially coherent beam through Selfoc fibers," Opt. Commun. **12**, 333–337 (1974).
22. G. P. Agrawal, "Imaging characteristics of square law media," Nouv. Rev. Opt. **7**, 299–303 (1976).
23. K. Iga, "Theory for gradient-index imaging," Appl. Opt. **19**, 1039–1043 (1980).
24. M. Conforti, C. M. Arabi, A. Mussot, and A. Kudlinski, "Fast and accurate modeling of nonlinear pulse propagation in graded-index multimode fibers," Opt. Lett. **42**, 4004–4007 (2017).
25. A. Ghatak and K. Thyagarajan, *An Introduction to Fiber Optics* (Cambridge University, 1999).
26. G. P. Agrawal, *Nonlinear Fiber Optics*, 6th ed. (Academic, 2019).
27. F. Matera, A. Mecozzi, M. Romagnoli, and M. Settembre, "Sideband instability induced by periodic power variation in long-distance fiber links," Opt. Lett. **18**, 1499–1501 (1993).
28. S. Roy, S. K. Bhadra, and G. P. Agrawal, "Effects of higher-order dispersion on resonant dispersive waves emitted by solitons," Opt. Lett. **34**, 2072–2074 (2009).
29. O. Tzang, A. Caravaca-Aguirre, K. Wagner, and R. Piestun, "Adaptive wavefront shaping for controlling nonlinear multimode interactions in optical fibres," Nat. Photonics **12**, 2665–2673 (2018).
30. E. Deliancourt, M. Fabert, A. Tonello, K. Krupa, A. Desfarges-Berthelemot, V. Kermene, G. Millot, A. Barthélémy, S. Wabnitz, and V. Couderc, "Wavefront shaping for optimized many-mode Kerr beam self-cleaning in graded-index multimode fiber," Opt. Express **27**, 17311–17321 (2019).